Bulletin of the Seismological Society of America, 89, 6, pp. 1606–1619, December 1999

Attenuation and Source Properties at the Coso Geothermal Area, California

by S. E. Hough, J. M. Lees, and F. Monastero

Abstract We use a multiple-empirical Green's function method to determine source properties of small (M −0.4 to 1.3) earthquakes and P- and S-wave attenuation at the Coso Geothermal Field, California. Source properties of a previously identified set of clustered events from the Coso geothermal region are first analyzed using an empirical Green's function (EGF) method. Stress-drop values of at least 0.5–1 MPa are inferred for all of the events; in many cases, the corner frequency is outside the usable bandwidth, and the stress drop can only be constrained as being higher than 3 MPa. P- and S-wave stress-drop estimates are identical to the resolution limits of the data. These results are indistinguishable from numerous EGF studies of M 2–5 earthquakes, suggesting a similarity in rupture processes that extends to events that are both tiny and induced, providing further support for Byerlee's Law. Whole-path Q estimates for P and S waves are determined using the multiple-empirical Green's function (MEGF) method of Hough (1997), whereby spectra from clusters of colocated events at a given station are inverted for a single attenuation parameter, κ, with source parameters constrained from EGF analysis. The κ estimates, which we infer to be resolved to within 0.01 sec or better, exhibit almost as much scatter as a function of hypocentral distance as do values from previous single-spectrum studies for which much higher uncertainties in individual κ estimates are expected. The variability in κ estimates determined here therefore suggests real lateral variability in Q structure. Although the ray-path coverage is too sparse to yield a complete three-dimensional attenuation tomographic image, we invert the inferred κ value for three-dimensional structure using a damped least-squares method, and the results do reveal significant lateral variability in Q structure. The inferred attenuation variability corresponds to the heat-flow variations within the geothermal region. A central low-Q region corresponds well with the central high-heat flow region; additional detailed structure is also suggested.

Introduction

The Coso, California, geothermal area located in east-central California (Fig. 1) has been the locus of bimodal volcanism over the past million years. The youngest radiometrically dated volcanic rocks yield an approximate age of 44,000 ± 22,000 years for the last eruptive episode. The geothermal area is located in the midst of a rhyolite dome field characterized by single endogenous domes, some of which still have associated tuff rings and explosion craters. The dome that is believed to be the youngest in the field, perhaps as young as 4000–6000 years, began steaming in December 1997 and continues steaming through early 1999.

The geothermal field has been the object of in-depth monitoring and geophysical analyses over the last two decades (e.g., Reasenberg *et al.,* 1980; Walter and Weaver, 1980), aimed at evaluation of an important energy resource and at a better scientific understanding of a tectonically complicated and intriguing region. Coso is situated in a transitional region between the right-lateral eastern Mojave shear zone associated with the North American and Pacific plate boundary system and the extensional Basin and Range region to the north and east. Focal mechanism studies generally indicate a mix of right-lateral and extensional solutions (e.g., Hauksson *et al.,* 1995).

A series of studies dating back to the 1980s have sought to provide a detailed image of the attenuation structure at Coso, driven in part by the expectation that significant variability in Q and velocity structure would be associated with the large inferred temperature variations (e.g., Young and Ward, 1980; Walck and Clayton, 1987; Ho-Liu *et al.,* 1988; Wu and Lees, 1996). These studies, which apply tomographic inversion techniques using as many as several thousand ray paths, have been successful in imaging three-dimensional variation in Q structure that can be associated with surface geology and heat-flow observations (e.g., Wu and Lees, 1996).

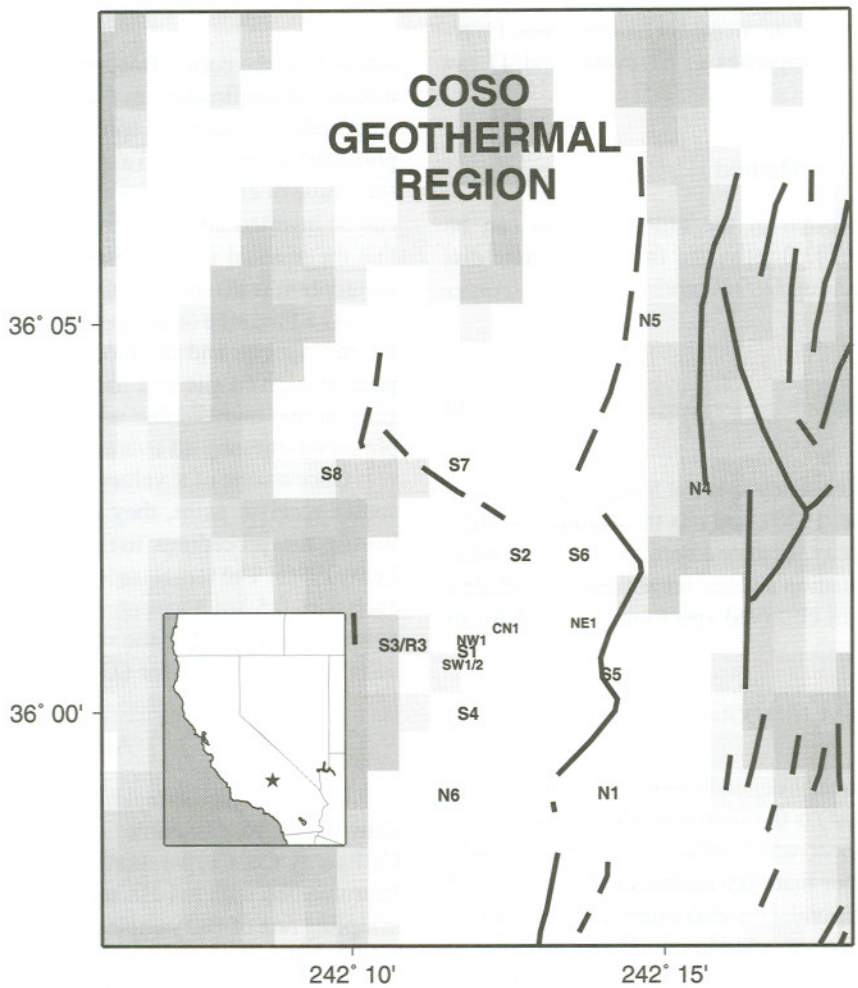

Figure 1. Map; Coso geothermal region and immediate surroundings. Station names are shown with larger type; smaller type indicates location of five clusters used in this study. Dashed and solid lines show mapped regional faults; topographic relief is (roughly) indicated with a gray scale. Small inset at left shows location of the Coso area within California.

In this study, we apply the multiple-empirical Green's function (MEGF) method to determine both attenuation and source properties in the region. The MEGF method has shown promise in reducing the considerable uncertainties that have typically been associated with attenuation estimates (Hough, 1997). These uncertainties arise from the trade-off between the inferred attenuation parameter, t^*, and the source controlled corner frequency, f_c (Anderson, 1986). As discussed by Hough (1997), considerable biases and uncertainties can arise even when joint inversion methods are used to determine attenuation and f_c. In addition to the trade-off between the two parameters, determination of f_c in the presence of even subtle site-response peaks can badly bias attenuation estimates.

The MEGF method provides several advantages: EGF deconvolutions (Mueller, 1985) allow high-resolution determination of f_c, unaffected by any site response short of nonlinear sediment behavior. Spectra from clusters of colocated events can then be used to determine a single path-dependent κ value, with the residual inferred to be site response. The determination of κ in the presence of site-response peaks is more robust than that of f_c, because the former is constrained by the shape of the spectrum over the entire bandwidth, while the latter can be pulled toward any isolated peak in the spectrum.

The MEGF method requires a specialized dataset of colocated events. Such events had been identified previously at Coso: Lees (1998) presents analysis of seven clusters of 9–17 events that are inferred to have source locations within tens of meters of each other. Lees (1998) concludes that these events are not true repeating earthquakes, but their spatial clustering is sufficiently tight (as we will show) for EGF analysis. In this article, we present analysis of five of these clusters. Two clusters from Lees (1998) are not analyzed here: NE2, which provides redundant ray-path coverage to the largest cluster analyzed (NE1), and CN2, which

also provides only redundant ray-path coverage as well as having a marginal range of moments for EGF analysis. Overall, we analyze source properties of 61 events and 47 ray paths.

Method

A detailed description of the MEGF method can be found in (Hough, 1997). Briefly, the far-field seismic displacement source spectrum $\Omega(f)$ is modeled by a one-corner model:

$$\Omega(f) = \frac{\alpha_o}{1 + (f/f_c)^c} \quad (1)$$

where α_0 is the low-frequency spectral level, f_c is the corner frequency (e.g., Brune, 1970), and c is the asymptotic high-frequency spectral decay, assumed here to be 2. The presence of apparent attenuation and site amplifications will alter equation (1) to give an observed spectrum $A(f, r)$ that can be generally written

$$A(f, r) = A_o(f)S(f)G(r)e^{-\pi f \int dr/Q\beta(r)} \quad (2)$$

where $S(f)$ is the frequency-dependent site term, $G(r)$ is geometrical spreading, $A_o(f)$ is the source acceleration spectrum $[f^2\Omega(f)]$, $\beta(r)$ is the shear-wave velocity along the ray path, and Q is a quality factor that may include both intrinsic and scattering losses. In general, Q is also expected to vary along the ray path (e.g., Anderson and Hough, 1984); it may also vary as a function of frequency. In this study, we will assume a frequency-independent Q (see Hough [1997] for further discussion). Under this assumption, Q is determined only from spectral shape (i.e., the asymptotic decay of the spectrum on log-linear axes); absolute amplitudes are not considered.

Equation (2) assumes correction for an instrument response term or that instrument response is flat within the frequency band of interest. To determine corner frequency, spectra estimated at discrete frequency points f_i from the jth and kth events are deconvolved to yield a relative source spectrum, R_{jk}:

$$R_{jk}(f_i, r) = \frac{\Omega_j(f_i)}{\Omega_k(f_i)} \quad (3)$$

That is, the common path and site effects cancel to isolate the relative source terms. If the corner frequencies are distinct from one another, estimates of equation (4) can be fit by a ratio of ω-square or ω-cube source spectra to obtain best-fitting corner frequency estimates for both events.

Once a set of f_c values is constrained, one can return to equation (3) and divide the observed spectra by the shape of the source spectrum to obtain a spectrum, $P_j(f_i)$, corrected for source spectral shape:

$$P_j(f_i) = A_j(f_i, r)[1 + (f/f_{cj})^c] = C_{oj}S(f_i)e^{-\pi\kappa f_i} \quad (4)$$

where f_{cj} is the corner frequency of the jth event. C_{oj} is now a constant amplitude term that will be affected by the source amplitude, geometrical spreading, and any Q_f that is proportional to frequency. Taking the logarithm of equation (5) for a suite of colocated events leads to a matrix equation that can be inverted linearly for C_{oj} and κ, under the assumption that the residual will correspond to the site term, $S(f_i)$. This assumption is discussed later in the article.

As a final step in the spectral analysis, residuals between the raw spectra and the models are calculated for all event pairs at a given site and then averaged. This procedure results in one unavoidable ambiguity: any common site amplification (among all events) cannot be resolved.

Once a suite of κ values are determined for all available source-receiver paths, they are inverted for attenuation following the procedures used (and described) by (Wu and Lees, 1996). The target region is divided into n by m blocks, each with 0.5-km horizontal extent. We use the 3D velocity model determined for the region by Lees (unpublished results, 1995) to invert for Q.

Analysis

The Coso geothermal field is monitored by a permanent network of 16 downhole instruments operated jointly by CalEnergy Co. Corporation and the U.S. Navy. Each site is instrumented with a 4-Hz sensor at 30–100 m depth, with a sampling rate of 480 samples/sec and an instrument response that is flat in velocity to 80 Hz. The configuration of the network has varied somewhat over its years of operation; in this study, we use data from the 12 stations shown in Figure 1. The availability of high-quality, low-noise data from a tightly clustered downhole array provides a unique opportunity to analyze attenuation structure and source parameters. The Coso region is also characterized by fairly high levels of earthquake swarm activity. The events analyzed here have estimated coda magnitudes (Andrews, 1986) ranging from −0.4 to 1.3 (see Lees, 1998).

Figure 2 shows one component of motion at a single station for one of the five event clusters that were judged to provide suitable event suites for analysis. Parameters for the events are listed in Table 1; locations of clusters are shown in Figure 1. To refer to a given cluster, we henceforth use the code listed in Table 1 (e.g., 'CN1'; corresponding to the designations of [Lees, 1998]). In most cases, events within a cluster are separated by less than 50 m laterally and a few hundred meters in depth. These events are considerably more tightly clustered than aftershock clusters typically used in EGF/MEGF analysis (e.g., Hough *et al.*, 1991; Hough, 1997).

To calculate spectra, we use windows of 450 and 150 samples (≈1 and ≈⅓ sec) bracketing the direct S and P arrivals, respectively. The choice of window length is necessarily somewhat subjective and must balance between

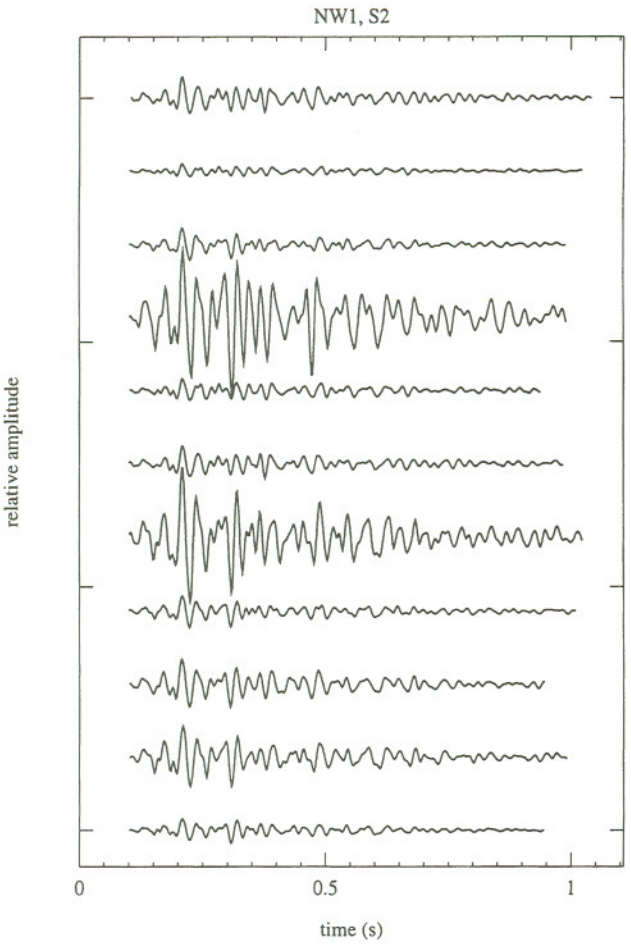

Figure 2. Scaled, offset north–south components of windowed *S*-wave traces for earthquakes in one cluster (NW1) used in this study. All traces are scaled by the same factor so that relative amplitudes shown are correct.

competing factors. For example, spectral estimates are generally more stable with longer windows, but there is a tradeoff with the amount of scattered energy that is included. Spectra are estimated using a multitaper method (Thompson, 1982; Park *et al.,* 1987) using seven 4π prolate windows, which produces an effective smoothing width of 4 Hz for *S*-wave spectra and 12 Hz for *P*-wave spectra. (The *P*-wave spectra are expected to be characterized by relatively low resolution, given the limitation imposed by the very short *S*-*P* times.) *P*-wave spectra are computed from the vertical component only; for the *S* waves, we calculate root-mean-square averages of the two horizontal components.

The largest two to three events within each cluster are used as mainshocks, with all other events being used as empirical Green's functions (Fig. 3). Deconvolutions are performed at all stations recording a given event pair. The resulting relative source spectra are then modeled with the ratio of theoretical ω-square models that yields an optimal least-squares solution as determined using a grid-search method.

The frequency-domain deconvolution yields relative source spectra that are, with few exceptions, well modeled by a ratio of ω-square spectra. In some cases, the deconvolution yields a spectral ratio that is nearly flat, indicating that the corner frequencies of two events are probably too similar to be distinguished. The frequency bandwidth for the EGF analysis is chosen for each event pair independently based on a visual inspection of the raw spectra. For *S*-wave spectra, a bandwidth of 5–80 Hz is generally used. For *P* waves, the shorter window lengths result in decreased resolution of spectra at low frequencies, and so the low-frequency cutoff is generally higher (5–15 Hz). In both cases, the low-frequency cutoffs are chosen relatively conservatively because the high high-frequency cutoff is felt to yield ample bandwidth with which to resolve κ.

In many cases, the relative source spectra do not exhibit flattening at high frequencies, indicating that the corner frequencies of these events is outside the usable bandwidth of the data. In these cases, an f_c value of 157 Hz is assigned, indicating a lower bound for the true value.

After all suitable pairs of events have been analyzed, final corner frequency estimates are made by averaging all available individual estimates. Standard deviations of f_c estimates can be made for both the mainshocks and Green's function events. For the small events, a standard deviation is estimated from all deconvolutions that use the event as an EGF, typically 6 to 8 stations for each of 1 to 3 mainshocks. These standard deviations are only meant to convey a general sense of consistency of individual f_c estimates; they are likely to be underestimates of the true standard deviations in some cases because they are estimated using the values of f_c that we determine only as lower bounds. That is, if individual corner frequency estimates vary between values below 157 Hz and the bounding value, the standard deviation will be underestimated. If all, or nearly all, of the individual estimates are at 157 Hz, then a low standard deviation only indicates that the true value is well resolved to be at least this high. For the overwhelming majority of events smaller than 10^{10} N·m, there is at best weak evidence that a corner frequency below 157 Hz is resolved (see Table 1).

For the mainshocks, f_c estimates are made using all EGF events at each station; the averages and (sample) standard deviations are calculated using dozens of individual f_c estimates (Table 1).

Once the corner frequencies are constrained, the velocity spectra are used in an inversion to find amplitude terms C_{oj} for each spectrum and a common path-dependent decay parameter, κ. For this calculation, we use spectra from all events within each cluster recorded at each station to obtain a single κ estimate for each source (cluster)-receiver path. Typically, 5 to 10 spectra are used in each inversion (Fig. 4).

This procedure yields spectral fits that are observed to be (subjectively) quite good in all cases. Optimal κ values in the range 0.01–0.05 sec are found for most paths. These values are determined over frequency ranges that vary depending on the observed noise level in each case. Most com-

Table 1

Source Properties

Cluster	Event	Year	Day	M_ox10^9	f_{cs}	sdev$_s$	N_s	f_{cp}	sdev$_p$	N_p
NE1	1	94	282	4.65	148*	16	15	150*	17	11
	2	94	282	3.40	156*	4	11	156*	3	9
	3	94	282	8.05	132*	29	16	157*	0	6
	4	94	282	4.16	154*	9	8		—	—
	5	94	282	2.98	157*	0	12	138*	34	11
	6	94	283	5.80	143*	24	14	145*	29	14
	7	94	283	18.3	54	14	83	54	18	76
	8	94	283	6.40	148*	22	11	151*	19	13
	9	94	284	12.4	—	—	—	157	0	5
	10	94	284	4.58	155*	9	14	149*	20	18
	11	94	284	2.61	155*	6	14	157*	0	9
	12	94	285	4.56	137*	31	19	151*	15	15
	13	94	285	12.6	61	13	73	63	20	62
	14	94	285	4.73	141*	28	14	141*	28	11
	15	94	288	2.37	154*	8	6	138*	31	7
	16	94	291	22.3	156*	2	6	155*	3	7
SW1	1	94	092	3.8	93*	46	9	151*	15	7
	2	94	118	6.0	125*	46	7	141*	30	8
	3	94	157	10.9	142*	21	6	157*	0	3
	4	94	157	134.0	52	19	21	53	14	14
	5	94	236	8.1	116*	39	15	118*	46	14
	6	94	297	9.8	129*	44	19	150*	23	20
	7	94	297	120.0	39	17	32	39	15	41
	8	94	297	40.0	119	46	6	117	42	4
	9	94	315	12.7	150	16	6	147	20	5
	10	94	316	94.6	51	17	28	49	19	17
	11	94	316	18.5	136*	37	12	139*	38	11
SW2	1	93	257	24.7	64*	42	6	126*	50	7
	2	93	285	15.7	84*	48	7	117*	40	8
	3	93	287	10.9	94*	52	6	97*	60	2
	4	93	290	19.2	94*	51	9	90*	55	5
	5	93	355	30.0	73*	49	4	63*	44	6
	6	93	359	66.9	75*	49	7	102*	44	8
	7	93	360	143.0	50	20	24	64.1	20.4	19
	8	93	360	28.6	82*	40	6	127*	30	2
	9	94	008	28.6	—	—	—	24	5	3
	10	94	011	182.0	29	17	21	47	24	22
NW1	1	93	322	145.0	39	14	44	43	13	31
	2	93	322	11.6	134*	27	7	157	0	5
	3	94	078	3.2	146*	26	14	149	15	11
	4	94	078	55.3	57	17	27	56	18	22
	5	94	078	1.51	142*	30	14	150*	26	13
	6	94	119	2.97	139*	32	18	140*	31	15
	7	94	119	2.67	135*	30	16	150*	21	11
	8	94	119	10.4	140*	35	6	139*	35	5
	9	94	256	16.0	123*	48	3	—	—	—
	10	94	269	4.5	123*	48	8	157*	0	1
	11	94	278	20.9	53	14	15	55	14	11
CN1	1	93	197	9.5	155*	4	8	157*	0	10
	2	93	246	22.0	157*	0	8	157*	0	9
	3	93	246	17.8	145*	28	7	153*	11	9
	4	93	310	3.6	156*	3	9	157*	0	9
	5	93	328	26.8	73	20	30	86	23	16
	6	93	328	5.4	149*	19	7	156*	2	5
	7	93	328	4.0	157*	1	10	153*	8	4
	8	94	079	13.7	51	14	29	55	10	37
	9	94	095	4.0	145*	24	8	157*	0	4
	10	94	095	1.6	157*	0	4	157*	0	4

Cluster; assigned event number; year and Julian day. Moments are determined by scaling relationship proposed by *Hanks and Boore*, (1984) using SCSN magnitudes; value listed is in N-m. f_{cs} and $sdev_s$ are average corner frequencies and standard deviations; N_s indicates number of individual deconvolved source spectra used to obtain each average f_c value. f_{cp}, $sdev_p$, and N_p are *P*-wave values. Asterisk * denotes f_c values that incorporate estimates that are lower bounds (see text).

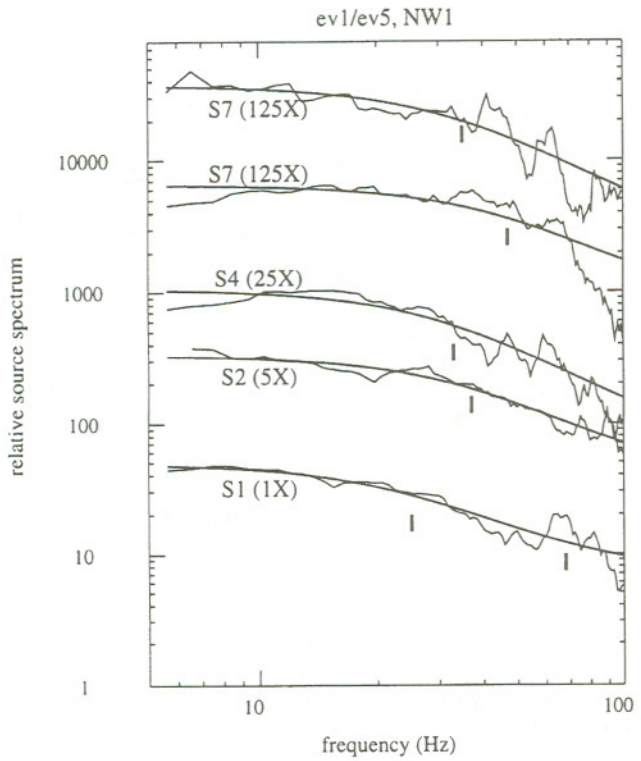

Figure 3. Deconvolved relative *S*-wave source (rms-averaged) spectra from one event pair within cluster NW1 at five stations. Source spectra are offset for clarity by the factor indicated next to each one. Solid line shows the best-fitting ratio of ω-square source models. Dark tick marks indicate corner frequency results; for all but the source spectrum from station S1, an f_c value greater than 100 Hz is obtained for the EGF event.

monly, a range of 5–80 Hz is used. For some high-attenuation paths, the range is as small as 5–35 Hz. Although it is difficult to fully quantify the uncertainties, the examples shown in Figure 4 illustrate the results for a range of κ values. We conclude that κ differences of 0.01 sec (i.e., the difference in values from S1 and S4, or R3 and S2) are easily resolved by the method.

As a final step, residuals are calculated between all spectra and models (Fig. 5). That is, under the assumption that the residual corresponds to the site-response term, the observed spectra are divided by the model incorporating both the source and attenuation results. This is done for each individual spectrum, and the results are then averaged within each cluster. For the *S* waves, residuals are systematically very small—generally varying by not more than approximately 20% and flat. These results indicate that equation (1) is successful in describing the observed *S*-wave spectral shapes, therefore validating the assumption that site response can be neglected in the determination of κ. This is encouraging but not surprising; because the data are recorded at borehole sites in mostly competent volcanic terrain, strong site effects are not expected.

P-wave residuals are perhaps more intriguing. Many of these are characterized by subtle peaks that are not reminiscent of resonance effects generated by amplification of waves in near-surface sediments (dark lines in Fig. 5; Kennett and Kerry, 1979). Rather, they exhibit a stair-step character, rising gradually over the span of 15–40 Hz to a peak before falling over the span of a few hertz, then often rising again. Although the *P*-wave spectra are heavily smoothed, the smoothing would not account for the asymmetric nature of the peaks. These observations are discussed in the following section.

The inferred *P*-wave residuals do raise the question of whether κ can be determined reliably in the presence of more substantial site response. There might, for example, be possible trade-offs between κ and a spectral peak at the lowest frequencies. Although the *P*-wave attenuation results might therefore be less reliable than the *S*-wave results, we note that many stations have comparable *P*- and *S*-wave residuals.

Interpretation: Attenuation, Source, and Site Effects

Stress Drop

To interpret the inferred corner frequency values for source parameters, we use the standard formulation (Keilis-Borok, 1959)

$$\sigma = M_o\left(\frac{f_c}{0.49\beta_s}\right)^3, \tag{5}$$

where β_s is the shear-wave velocity at the source (assumed here to be 3.2 km/sec) and σ is an estimate of dynamic stress drop that can be equated (under assumptions regarding the source model) to static stress drop (e.g., Brune, 1970). The seismic moment M_0, is estimated using the moment-magnitude relationship developed by Hanks and Boore (1984), $\log(M_0) = 1.5M + 9.1$, where it is assumed that the local network magnitude provides an estimate of the moment magnitude, and moment is in N·m.

S- and *P*-wave stress-drop values for all events are shown in Figure 6a and 6b. We observe no systematic differences between the different clusters, except that, as one would expect, stress-drop values for the clusters with relatively larger overall magnitudes are better resolved. The stress-drop results bear a striking similarity to those determined with EGF analysis for *M* 2–5 aftershocks of the Joshua Tree earthquake (e.g., Hough and Dreger, 1995): the well-constrained values for the larger events (here *M* 0.5–1) are all between 0.5 and 10 MPa. For events smaller than *M* 0.5, stress drop can generally only be constrained to be above the value indicated by the lines in Figure 6 (i.e., that the corner frequency is too far above the usable bandwidth to be resolved). These results provide evidence that similarity in earthquake rupture processes extends to events as small as *M* 0 and to events that are induced by injection.

The ratio between *S*- and *P*-wave stress-drop values ex-

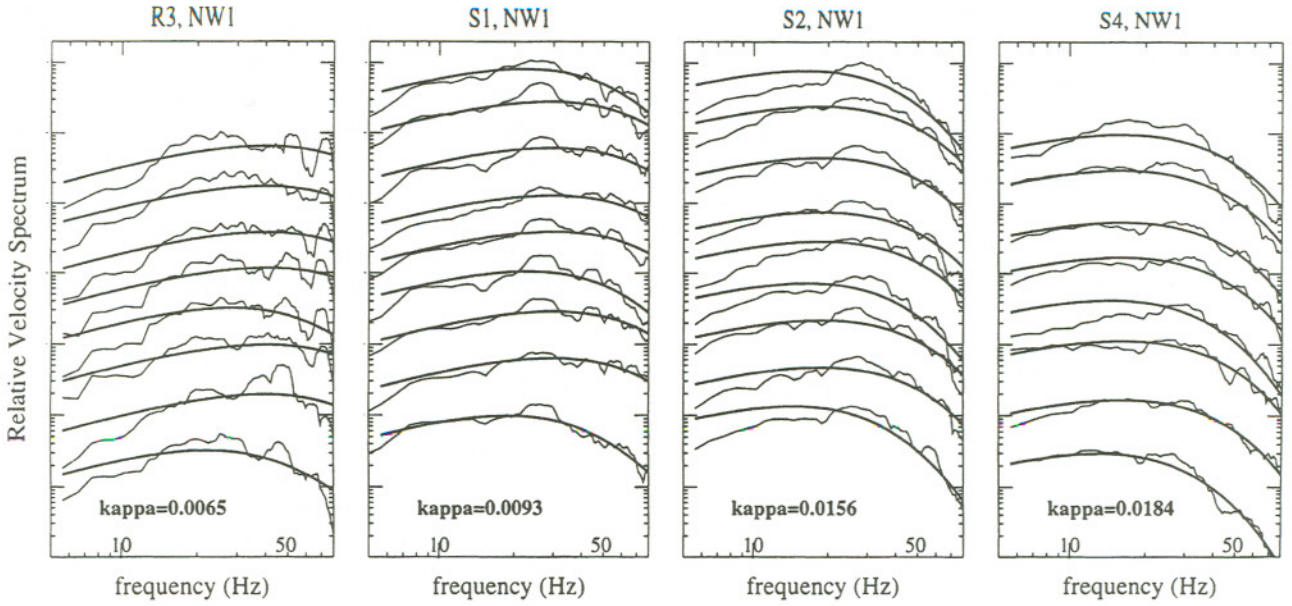

Figure 4. Estimated (uncorrected) relative *S*-wave velocity spectra (rms average of two horizontal components) are shown for events from cluster NW1 recorded at four stations: R3 (far left), S1 (near left), S2 (near right), S4 (far right). In each panel, solid line gives best-fitting model with corner frequency constrained from empirical Green's function analysis and common κ value fit by simultaneous inversion of all spectra in each cluster. Spectra are offset vertically for clarity.

hibits some scatter but is centered around a value of 1 (Fig. 7a). (Figure 7a does not include three points considered outliers, with ratios between 2.3 and 3.8.) The distribution of ratios (Fig. 7b) perhaps suggests a tendency toward ratios slightly less than 1, but with more high than low outliers. Considering all of the data, the average ratio is found to be 1.05 ± 0.58. Discarding the three high outliers, one obtains 0.93 ± 0.31. Given the uncertainties in either case, we conclude that the results do not resolve a ratio different than 1.

Attenuation

The inferred *S*-wave κ values from the Coso events are shown as a function of epicentral distance in Fig. 8 (*P*-wave values are similar). The values are characterized by a general increase with distance, as expected. As discussed by Anderson and Hough, (1984), a simple Q model incorporating a low near-surface Q value and a higher regional Q at depth will give rise to a finite value of the intercept $\kappa(0)$ and a linear slope of $d\kappa/dr$.

The $\kappa(r)$ values estimated here exhibit a degree of scatter that is comparable to that obtained for other regions using single-spectrum methods (e.g., Hough and Anderson, 1988). Although Figure 8 includes results from all stations, we observe no systematic differentiation of κ values between the different stations. This is perhaps not surprising given that the estimates are made from borehole data.

If a straight line were fit to the $\kappa(r)$ points shown in Figure 8, a scatter on the order of ±0.01 sec would result. Considering that the inferred resolution of κ estimates from individual cluster-station pairs is better than 0.01 sec, this suggests that the scatter evident in Figure 8 may reflect real lateral variability in attenuation structure.

Although the ray-path coverage is too sparse to allow a true tomographic attenuation model to be determined, we invert the κ values for both *S* and *P* waves using the damped least-squares method described by Wu and Lees (1996). The inversions are calculated over 0.5-km-depth intervals and resampled to obtain the three-layer Q_s and Q_p models shown in Figure 9. The Q_s and Q_p results are found to be strikingly similar, perhaps providing an added measure of confidence that the MEGF approach is able to determine κ reliably even given the relatively stronger inferred *P*-wave site response.

Clearly, the best ray-path coverage is available for the middle depth layer, 1–2 km. For both *S* and *P* waves, a central low Q corresponds very well with the extent of the production field (encompassed by the inner stations, S1–S6). The Coso geothermal field is a high–heat-flow region within which a brittle– ductle transition of approximately 5 km has been inferred (Feng and Lees, 1998). That is, the depth of the brittle–ductle transition domes sharply upward in the immediate vicinity of the field.

The sparse images provide hints of more detailed variation in attenuation structure. In general, it is striking that the attenuation in the 0–1-km layer is generally lower than at 1–2 km, with the possible exception of the southern edge of the region. This contrasts with previous $Q(z)$ results in other regions that nearly universally find a near-surface layer in which Q is dramatically lower than at depth, even in gra-

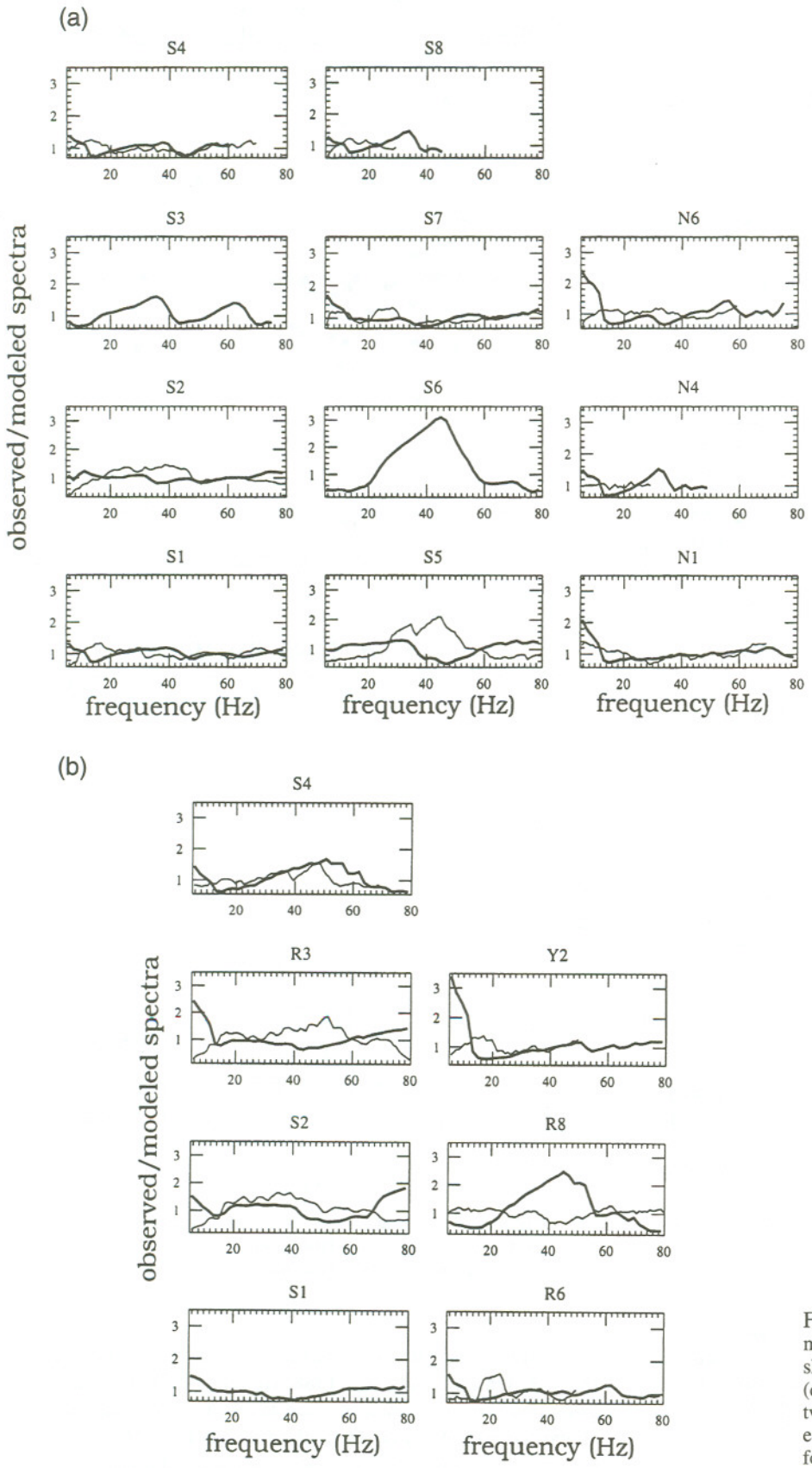

Figure 5. (a) Residuals between spectra and models for cluster NE1 at each station are shown for *S* waves (light lines) and *P* waves (dark lines). For each station, residuals between spectra and models are averaged over all events within the cluster. (b) Same as (a), but for cluster CN1.

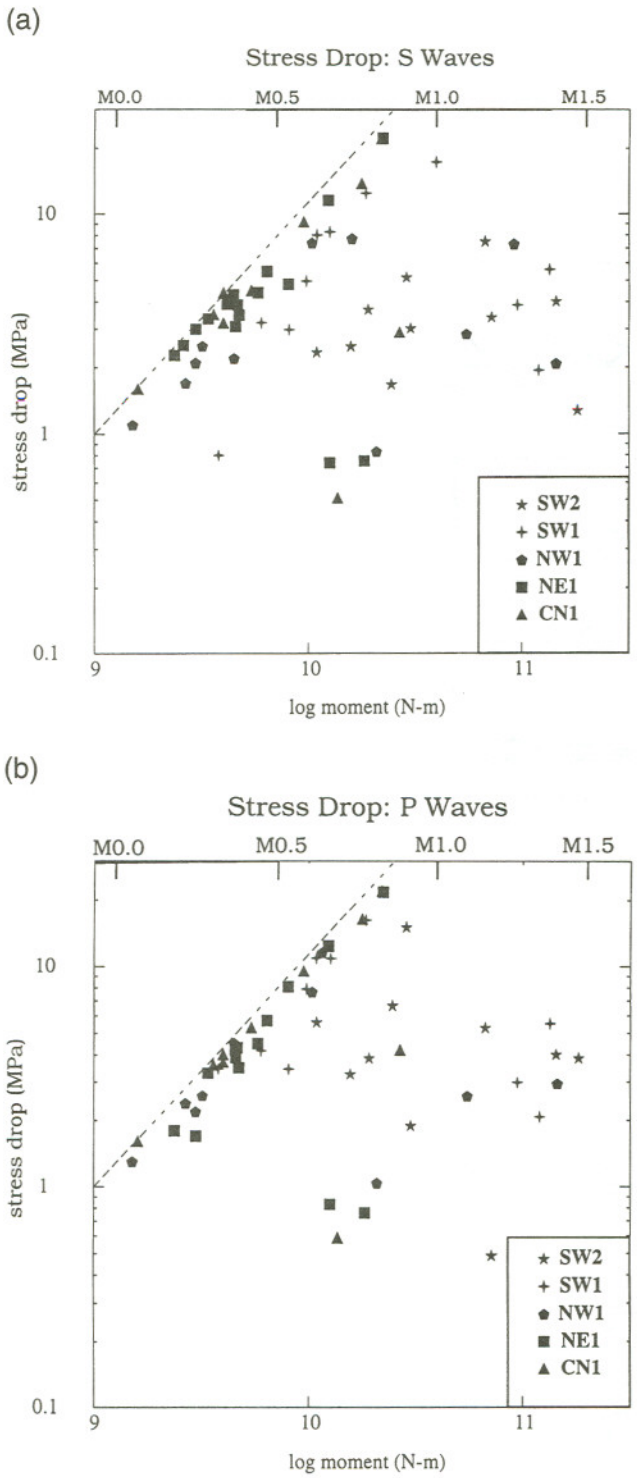

Figure 6. (a) *S*-wave stress-drop values for all events for all events analyzed. Symbols correspond to different clusters as shown in the legend. Dashed line corresponds to an f_c value of 157 Hz; results approaching this value are at best only weakly constrained by the data and can be considered lower bounds. (b) Same as (a) for *P* waves.

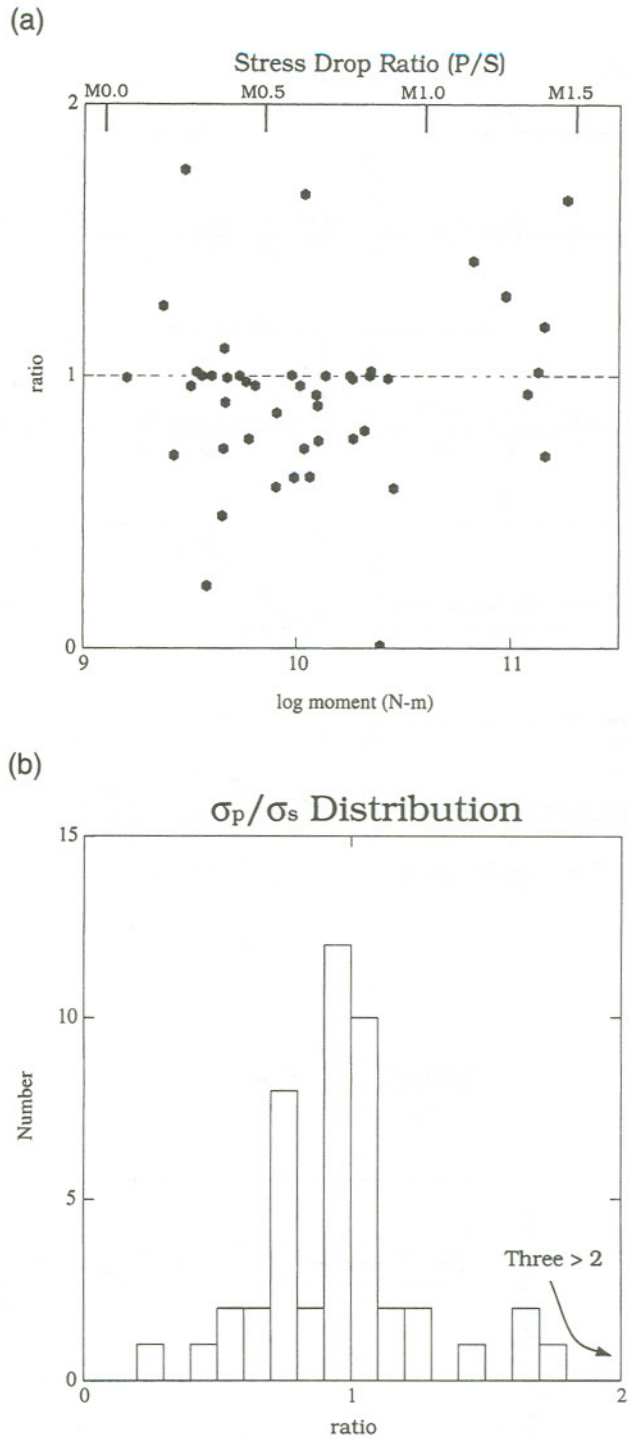

Figure 7. (a) Ratio of *S*- to *P*-wave stress-drop values for all events. (b) Histogram of σ_p/σ_s results, excluding three values considered outliers.

nitic terrain where low near-surface attenuation is expected (e.g., Hough and Anderson, 1988; Hough, 1997). This suggests that the low-*Q* near-surface layer at Coso is largely above the 30–100 m depth of the instruments. (The alternative, that no low-*Q* region exists, is considered less likely.)

At 2–3 km depth, the most striking feature of both the

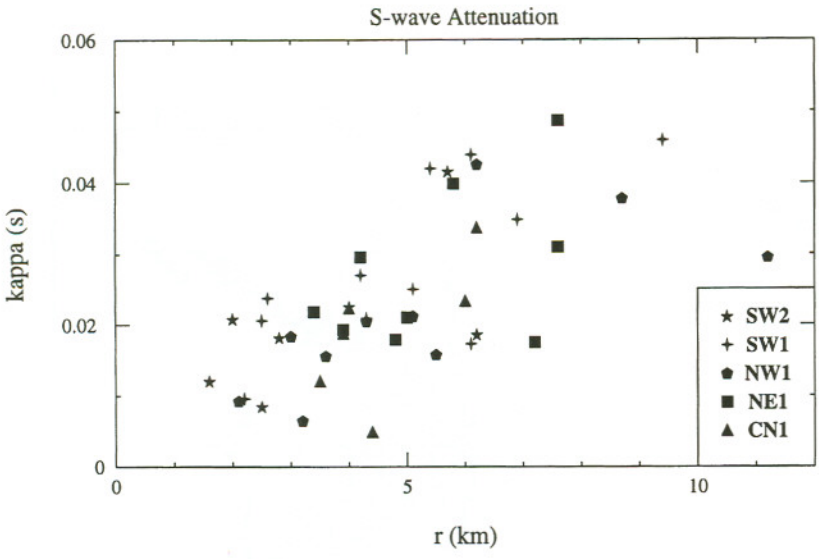

Figure 8. The inferred *S*-wave κ values are plotted as a function of hypocentral distance for all cluster–station pairs analyzed. A different symbol is used to denote κ values at each station.

P- and *S*-wave models is a low-Q region toward the northeast edge of the region. This eastward shift of the low-Q zone with depth is coincident with a shift in the depth of production zones in the geothermal wells. Wells located between stations S6 and S5 produce maximum high-temperature fluids from minimum depths of 3 km. In the central part of the field, the main production zone is at 1.5–2.5 km depth.

It is interesting to note that, in terms of absolute amplitudes, the low-Q region in the northeast corner of the field is more prominant in the Q_p image than the Q_s results. Laboratory measurements generally predict Q_p/Q_s ratios greater than 1 for water-saturated rock (e.g., Toksoz *et al.,* 1978). The result $Q_p < Q_s$ in the low-Q northeastern anomaly suggests that this anomaly results from a heat-controlled attenuation mechanism rather than a fluid-controlled one. In general, the fact that our Q_p and Q_s values are comparable suggests that rocks within the geothermal region are not pervasively saturated.

Site Response

The spectral residuals presented in Figure 5 are expected to incorporate a number of unmodeled effects, including possible differences in source depth and focal mechanism between an earthquake and its EGF event. However, the inferred *S*-wave residuals are of uniformly low amplitude, generally varying by less than 20%.

The *P*-wave residuals are more intriguing. They show significant variation around unity, with a common suggested character. The stair-step shape (Fig. 5) is not consistent with an expected one-dimensional site response in a low-velocity layer (Kennett and Kerry, 1979). However, these spectra do bear some resemblance to theoretically predicted trapped waves in fluid-filled cracks or conduits (Ben-Zion, 1998).

Although trapped waves are potentially of great utility in resolving the nature of fault zone structure (Ben-Zion, 1998), we observe them to be a fairly pervasive characteristic of *P*-wave residuals in our dataset. No strong associations are observed between the paths for which strong trapped waves are suggested and the mapped faults shown in Figure 1. We thus hypothesize that either (1) trapped waves are generated within the drill holes, creating a strong *P*-wave signature that is broadly observed over the area spanned by the array, or (2) the *P*-wave residuals in fact result from some process other than site response or fault-zone waves.

Discussion and Conclusions

We have applied the multiple-empirical Green's function method to a dataset comprised of 61 events recorded at 5–10 stations apiece. Our results confirm those obtained by Hough (1997) for a much smaller dataset: that the MEGF approach provides high-resolution estimates of path-dependent attenuation estimates and site response. The simple model—a one-corner source spectrum and a frequency-independent Q—is found to be adequate to model the spectral shape of events with magnitudes between -0.4 and 1.3.

Corner frequency results imply stress-drop values almost exclusively in the range of 1–20 MPa, with no resolved scaling of stress drop with moment. Stress-drop estimates of the larger events within this dataset, that is, those of $\log(M_o) > 10.5$ (N·m) are well resolved and all within an even narrower range, roughly 2–8 MPa. For events smaller than $\log(M_o) = 10$, our results only yield 1 MPa and upward as a lower bound on stress drop.

The stress-drop values obtained for the small Coso events substantiates the overall conclusions of Abercrombie and Leary (1993), that similarity of rupture processes extends to events as small as 10^7–10^9 N·m. However, there is the suggestion of a systematic increase in stress drop in the compiled results shown in the earlier study (their Fig. 5)

(a)

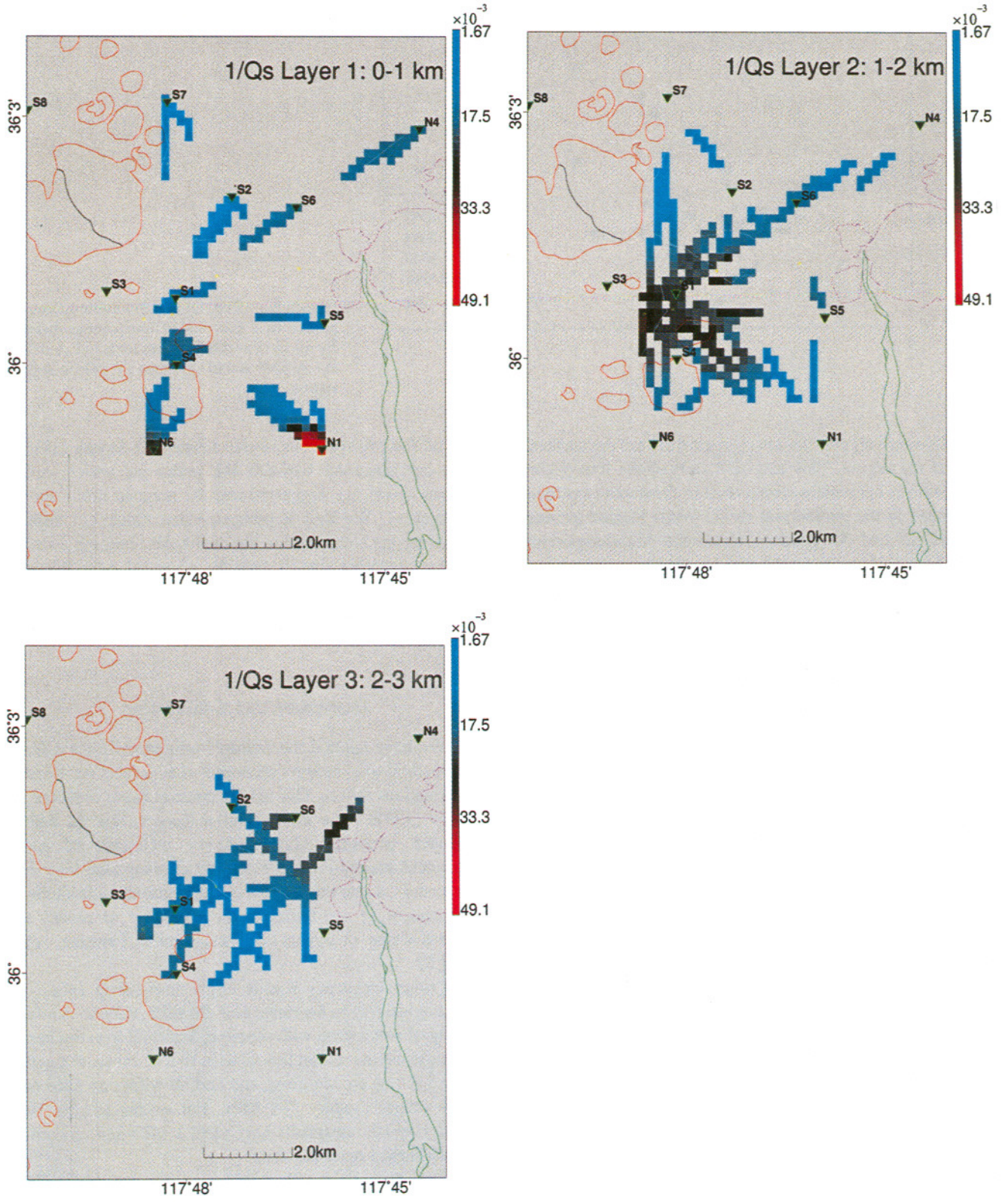

Figure 9. (a) Resampled tomographic results for Q_s^{-1} structure. Red indicates lowest Q_s values; blue indicates highest. Results are shown for 0–1 km (*top left*), 1–2 km (*top right*), and 2–3 km (*bottom left*). Seismic stations are indicated with inverted triangles. Thin red lines indicate rhyolite domes; thin green line indicates quaternary basaltic lava flow (Duffield and Bacon, 1981). *Caption continues on next page.*

(b)

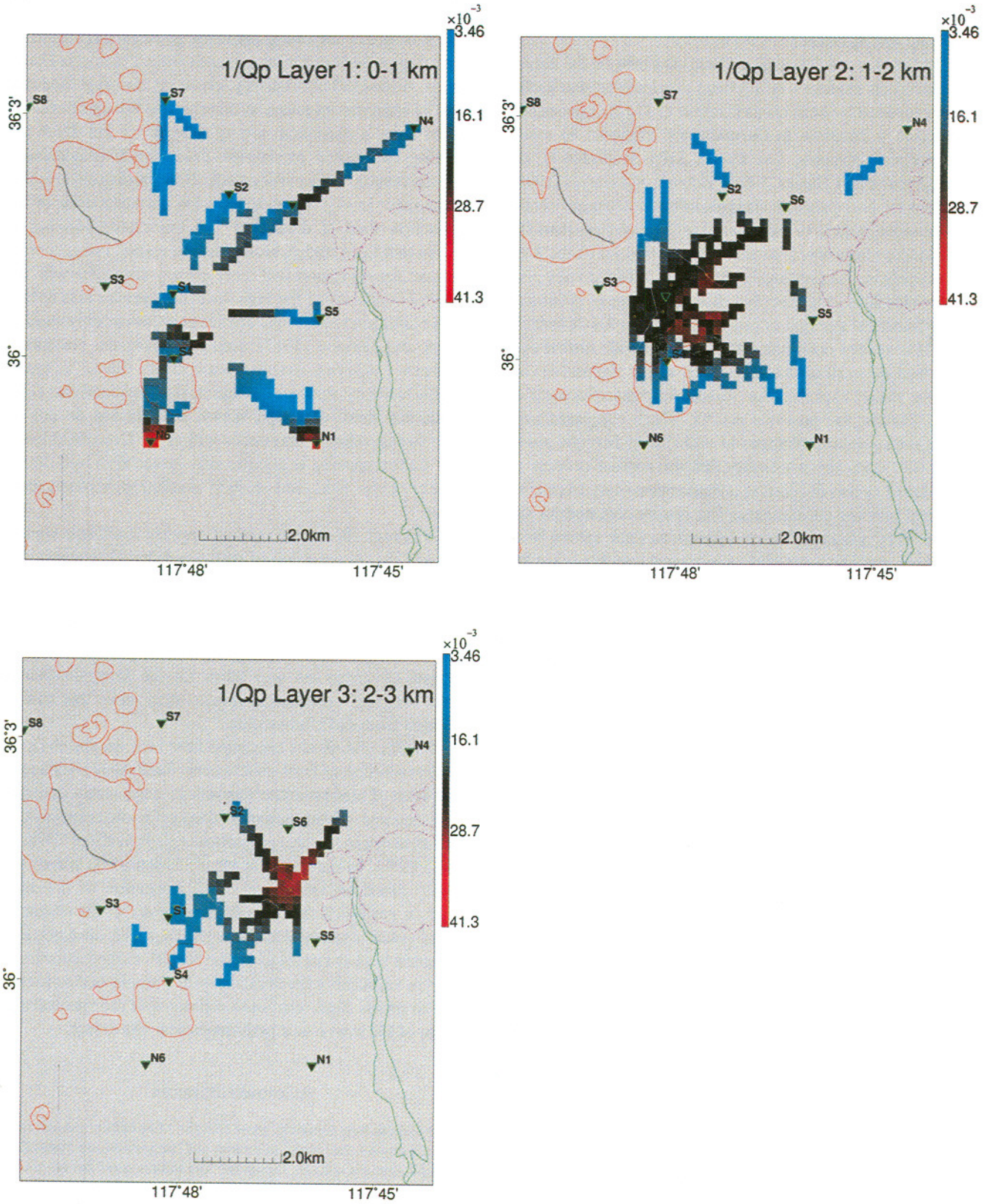

Figure 9. (*continued*) (b) Same as (a) but for Q_p^{-1}.

between a magnitude range of roughly −2 to 5. The results obtained here provide additional evidence that stress-drop values for smaller events do span a similar range as those of moderate earthquakes.

The source results obtained here also bear on the nature of induced earthquakes. It has been documented that earthquakes induced by both oil production and brine injection at a 9-km-deep borehole in Germany are triggered by small pore pressure changes, less than 1 MPa (Rutledge *et al.,* 1998; Zoback and Harjes, 1998). Zoback and Harjes (1998) note that the pore pressure changes inferred to trigger events similar in magnitude to those analyzed here are less than 1% the ambient stress levels expected at the bottom of the KTB deep borehole. As previously discussed, these studies provide compelling evidence that differential stress is limited by the frictional strength of pre-existing fractures (Byerlee's Law). The results obtained in this study provide further evidence that the earthquake stress-drop values themselves reflect the range expected for rupture of faults/fractures at depth. That is, the previous results, which compared triggering pore pressure changes to ambient hydrostatic stress levels, left open the possibility that the rupture process of the induced events differed in a fundamental way from non-triggered tectonic earthquakes. The results obtained for the Coso events, although from a different tectonic setting from the others, provide a measure of evidence that this is not the case and thus provide an added measure of support for Byerlee's Law.

Our corner frequency estimates also bear on the issue of fracture density within the geothermal field. In the previous analysis of these multiplet data, Lees (1998) attempted to estimate the crack density by dividing the surface area of fractures observed in a narrowly defined volume determined by the multiplet distribution. Following Andrews (1986), the crack radius is estimated by

$$r = \frac{2.34v}{2\pi f_c}, \tag{6}$$

where $v = 3.0$ km/sec is the average velocity and f_c is the corner frequency. The new estimates of f_c will change our earlier estimates of the crack radii. Using an average $f_c = 150$ Hz, we get an average crack radius of 7.5 m. This is about a quarter of the estimate Lees (1998) obtained earlier, which translates into an average fracture density approximately 1/16 of Lees' original estimate. The underestimation of f_c was acknowledged in Lees (1998); here we can offer an appropriate correction.

The new estimate of crack density is 0.011 m^2/m^3, an order of magnitude smaller than previously reported. The new results seem to be in better agreement with estimates of crack density determined by Shalev and Lou (1995), who used observations of shear-wave anisotropy and splitting to infer a maximum crack density of 0.035 at 2 km depth within the Coso geothermal field.

The attenuation results obtained in this study can be compared with previous studies in the Coso geothermal region. In a recent investigation, Wu and Lees (1996) obtained a three-dimensional tomographic image of attenuation structure using pulse-broadening methods from 838 microseismic events. Although our relatively sparse ray coverage does not yield as complete an image as obtained by Wu and Lees, our results show a prominent low-Q zone at ≈1 km depth underlying the central production field, which is consistent with the results of the earlier study. Both studies also resolve a prominent low-Q region toward the northeast edge of the production field at depths of 2–3 km (2.44–3.66 km in the Wu and Lees study). However, our results image a more compact low-Q region that more closely coincides with the known boundaries of the high–heat-flow production field.

In addition to previous attenuation tomography studies, Walck and Clayton (1987) used data from the permanent Southern California seismic network to obtain a tomographic velocity image of a region that included the Coso geothermal field. Although Walck and Clayton do not resolve strong velocity anomalies within the Coso field itself, their station spacing is significantly larger than ours in the vicinity of the field, and so their resolution is much more coarse.

Although the MEGF method appears to offer a significant increase in precision of path-dependent attenuation estimates, the trade-off is the relatively more labor-intensive methodology that can make it prohibitive to analyze large numbers of events. However, the MEGF approach is clearly tenable in regions where available sources provide adequate ray-path coverage and may allow for the determination of more "surgical" attenuation images than those that can be obtained from more noisy data.

Finally, the results presented here bear on the observational resolution of fault-zone waves. Fault-zone (FZ) waves have been of interest in the seismology community in recent years because of the potential they offer on constraint of fault-zone geometry and properties (e.g., Ben-Zion, 1998; Li *et al.,* 1998). In the past, the identification of FZ waves has largely relied on subjective visual inspection of raw time series or perhaps a fairly crude assessment of the character of individual spectra. Although the FZ wave interpretation presented here is speculative, the MEGF method appears to offer an approach whereby data from a single station can be used to obtain high-resolution estimates of the spectral signature of FZ waves as a path-dependent site effect.

Acknowledgments

We thank Joan Gomberg, Steve Hartzell, Mike Fehler, and two anonymous reviewers for helpful comments and suggestions; we thank Peter Malin for data and valuable comments. The authors thank the Navy Geothermal Program for funding J. Lees' efforts on this project (Awards N68936-94-R-0139 and N68936-97-C-0001). We further acknowledge CalEnergy Co. Inc. for making available their data. Figure 1 was generated using GMT software (Wessel and Smith, 1991); Figures 9a and 9b were generated using Xmap8 (Lees, 1995).

References

Abercrombie, R., and P. C. Leary (1993). Source parameters of small earthquakes recorded at 2.5 km depth, Cajon Pass, California: implications for earthquake scaling, *Geophys. Res. Lett.* **20,** 1511–1514.

Anderson, J. G. (1986). Implication of attenuation for studies of earthquake source, in *Earthquake Source Mechanics,* S. Das and C. H. Scholz (Editors), American Geophysical Monograph 37, 311–318.

Anderson, J. G., and S. E. Hough (1984). A model for the shape of the Fourier amplitude spectrum of acceleration at high frequencies, *Bull. Seism. Soc. Am.* **74,** 1969–1994.

Andrews, D. J. (1986). Objective determination of source parameters and similarity of earthquakes of different size, in *Earthquake Source Mechanics,* S. Das and C. H. Scholz (Editors), American Geophysical Monograph 37, 259–267 (1998).

Ben-Zion, Y. (1998). Properties of seismic fault zone waves and their utility for imaging low-velocity structures, *J. Geophys. Res.* **103,** 12567–12585.

Brune, J. N. (1970). Tectonic stress and the seismic shear waves from earthquakes, *J. Geophys. Res.* **75,** 4997–5009.

Duffield, W. A., and C. R. Bacon (1981). Geologic map of the Coso volcanic field and adjacent areas, Inyo County, California, U.S. Geol. Surv. Misc. Invest. Ser., MAP-1200.

Feng, Q., and J. M. Lees (1998). Microseismicity, stress, and fracture within the Coso geothermal field, California, *Tectonophysics* **289,** 221–238.

Hanks, T. C., and D. Boore (1984). Moment-magnitude relations in theory and practice, *J. Geophys. Res.* **89,** 6229–6235.

Hauksson, E., K. Hutton, H. Kanamori, L. Jones, J. Mori, S. Hough, and G. Roquemore (1995). Preliminary report on the 1995 Ridgecrest earthquake sequence in eastern California, *Seism. Res. Lett.* **66,** 54–60.

Ho-Liu, P., H. Kanamori, and R. W. Clayton (1988). Application of attenuation tomography to Imperial Valley and Coso-Indian Wells region, southern California, *J. Geophys. Res.* **93,** 10501–10520.

Hough, S. E. (1997). Empirical Green's function analysis: taking the next step, *J. Geophys. Res.* **102,** 5369–5384.

Hough, S. E., and J. G. Anderson (1988). High-frequency spectra observed at Anza, California: implications for Q structure, *Bull. Seism. Soc. Am.* **78,** 692–707.

Hough, S. E., and D. S. Dreger (1995). Source parameters of the 4/23/92 Joshua Tree, California, earthquake and its aftershocks: empirical Green's function analysis of TERRAscope and GEOS data, *Bull. Seism. Soc. Am.* **85,** 1576–1590.

Hough, S. E., L. Seeber, A. Lerner-Lam, J. G. Armbruster, and H. Guo (1991). Empirical Green's function analysis of Loma Prieta aftershocks, *Bull. Seism. Soc. Am.* **81,** 1737–1753.

Keilis-Borok, V. I. (1959). On the estimation of the displacement of an earthquake source and of source dimension, *Ann. Geofis.* **12,** 205–214.

Kennett, B. L. N., and N. J. Kerry (1979). Seismic waves in a stratified half space, *Geophys. J. R. Astr. Soc.* **57,** 557–583.

Lees, J. M. (1995). Xmap8: three-dimensional GIS for geology and geophysics, *Seism. Res. Lett.* **66,** 33–37.

Lees, J. M. (1998). Multiplet analysis at Coso Geothermal, *Bull. Seism. Soc. Am.* **88,** 1127–1143.

Li, Y.-G., K. Aki, J. E. Vidale, and M. G. Alvarez (1998). Delineation of the Nojima fault ruptured in the M7.2 Kobe, Japan, earthquake of 1995 using fault zone trapped waves, *J. Geophys. Res.* **103,** 7247–7263.

Mueller, C. S. (1985). Source pulse enhancement by deconvolution of an empirical Green's function, *Geophys. Res. Lett.* **12,** 33–36.

Park, J., C. Lindberg, and F. L. Vernon III (1987). Multitaper spectral analysis of high-frequency seismograms, *J. Geophys. Res.* **92,** 12675–12684.

Reasenberg, P., W. Ellsworth, and A. Walter (1980). Teleseismic evidence for a low-velocity body under the Coso geothermal area, *J. Geophys. Res.* **85,** 2471–2483.

Rutledge, J. T., W. S. Phillips, and W. S. Schuesster (1998). Reservoir characterization using oil-production-induced microseismicity, Clinton County, Kentucky, *Tectonophysics* **289,** 129–152.

Shalev, E., and M. Lou (1995). Tomographic inversion for crack-density in Coso, California, *EOS* **76,** 351.

Thompson, D. J. (1982). Spectrum estimation and harmonic analysis, *IEEE Proc. 70,* 1055–1096.

Toksoz, M. N., A. H. Johnston, and A. Timur (1978). Attenuation of seismic waves in dry and saturated rocks. I. Laboratory measurements, *Geophysics* **44,** 681–690.

Walck, M. C., and R. W. Clayton (1987). P-wave velocity variations in the Coso region derived from local earthquake travel times, *J. Geophys. Res.* **92,** 393–405.

Walter, A. W., and C. S. Weaver (1980). Seismicity of the Coso Range, California, *J. Geophys. Res.* **85,** 2441–2458.

Wessel, P., and W. H. F. Smith (1991). Free software helps map and display data, *EOS* **72,** 441–446.

Wu, H., and J. M. Lees (1996). Attenuation structure of Coso geothermal area, California, from wave pulse widths, *Bull. Seism. Soc. Am.* **86,** 1574–1590.

Young, C. Y., and R. W. Ward (1980). Three-dimensional Q^{-1} model of the Coso Hot Springs known geothermal resource area, *J. Geophys. Res.* **85,** 2459–2470.

Zoback, M. D., and H. P. Harjes (1998). Injection-induced earthquakes and crustal stress at 9-km depth at the KTB-deep-drilling-site Germany, *J. Geophys. Res.* **102,** 18477–18491.

United States Geological Survey
Pasedena, California
(S.E.H.)

Yale University
New Haven, Connecticut
(J.M.L.)

U.S. Navy Geothermal Program
China Lake, California
(F.M.)

Manuscript received 15 April 1999.